ACS APPLIED MATERIALS & INTERFACES

Biological and Medical Applications of Materials and Interfaces

PEGylation of paclitaxel-loaded cationic liposomes drives steric stabilization of bicelles and vesicles thereby enhancing delivery and cytotoxicity to human cancer cells

Victoria Marie Steffes, Zhening Zhang, Scott MacDonald, John Crowe, Kai K Ewert, Bridget Carragher, Clinton S. Potter, and Cyrus R Safinya

ACS Appl. Mater. Interfaces, **Just Accepted Manuscript** • DOI: 10.1021/acsami.9b16150 • Publication Date (Web): 10 Dec 2019

PEGylation of paclitaxel-loaded cationic liposomes drives steric stabilization of bicelles and vesicles thereby enhancing delivery and cytotoxicity to human cancer cells

Victoria M. Steffes[1,2], Zhening Zhang[3,4], Scott MacDonald[5], John Crowe[5], Kai K. Ewert[1], Bridget Carragher[3], Clinton S. Potter[3], Cyrus R. Safinya*[1,5,6]

[1]*Materials Department, University of California, Santa Barbara, California 93106, USA*
[2]*Chemistry and Biochemistry Department, University of California, Santa Barbara, California 93106, USA*
[3]*The National Resource for Automated Molecular Microscopy, Simons Electron Microscopy Center, New York Structural Biology Center, New York, NY 10027, USA*
[4]*Present Address: Biochemistry and Molecular Biophysics Department, Columbia University Medical Center, New York, NY 10032, USA*
[5]*Physics Department, University of California, Santa Barbara, California 93106, USA*
[6]*Molecular, Cellular, and Developmental Biology Department, University of California, Santa Barbara, California 93106, USA*
*Corresponding author: safinya@mrl.ucsb.edu

Abstract

Polyethylene glycol (PEG) is a polymer used widely in drug delivery to create "stealth" nanoparticles (NPs); PEG coatings suppress NP detection and clearance by the immune system and beneficially increase NP circulation time *in vivo*. However, NP PEGylation typically obstructs cell attachment and uptake *in vitro* compared to the uncoated equivalent. Here, we report on a cationic liposome (CL) NP system loaded with the hydrophobic cancer drug paclitaxel (PTX) in which PEGylation (i.e. PEG-CL_{PTX} NPs) unexpectedly enhances, rather than diminishes, delivery efficacy and cytotoxicity to human cancer cells. This highly unexpected enhancement occurs even when the PEG-chains coating the NP are in the transition regime between the mushroom and brush conformations. Cryogenic TEM of PEG-CL_{PTX} NPs shows that PEG causes the proliferation of a mixture of sterically stabilized nanometer-scale vesicles and anisotropic micelles (e.g. bicelles). Remarkably, the onset of bicelles at sub-monolayer concentrations of the PEG-coat has to our knowledge not been previously reported; it was previously thought that PEG-lipid in this composition regime was incorporated into vesicles but did not alter their shape. Confocal microscopy and flow cytometry reveal significantly greater PTX cell uptake from stabilized PEG-CL_{PTX} NPs (vesicles and bicelles) in contrast to bare CL_{PTX} NPs, which can aggregate in cell medium. This underscores the ability of steric stabilization to facilitate NP entry into cells via distinct size-dependent

endocytic pathways, some of which cannot transport large NP aggregates into cells. This study highlights the value of understanding how PEGylation alters NP shape and structure, and thus NP efficacy, to design next-generation stealth drug carriers that integrate active cell-targeting strategies into NPs for *in vivo* delivery.

Introduction

Hydrophobic paclitaxel (PTX) is a widely-used cancer chemotherapy drug for treating ovarian, breast, lung, pancreatic, and other cancers and is included in the World Health Organization's List of Essential Medicines[1–10]. PTX is a mitotic inhibitor that halts the proliferation of tumor cells by disrupting the cell cycle and induces cell death[2,11]. Since 1992, PTX has been administered in hospitals in the patented formulation Taxol whose solvents (polyethoxylated castor oil and ethanol) cause hypersensitivity reactions requiring premedication in addition to side-effects from the PTX drug itself[12–14]. More recently, the (non-targeted) albumin nanoparticle (NP) formulation Abraxane has been used as a Taxol alternative to eliminate drug-carrier toxicity, but has demonstrated mixed results in terms of improved patient outcomes[15–17]. Several alternative formulations for PTX delivery, using either liposomes (closed membrane shells) or polymeric NPs, have been approved outside of the U.S. or are in clinical trials[14], with many more in preclinical development[18]. To substantively improve the therapeutic efficacy of PTX, it needs to be administered by a non-toxic solubilizing agent that is capable of tumor-specific targeted delivery, which concentrates the cytotoxic drugs where they are needed and minimizes their accumulation in healthy tissue[19–21].

Liposomes are among the most investigated synthetic carriers of cytotoxic hydrophobic drugs in cancer therapeutics worldwide[22–30]. Lipid NPs are suitable drug delivery vehicles for hydrophobic drugs and decrease side effects compared to established solvent systems (such as Cremophor EL in Taxol)[14,31,32]. It is useful to note here that the widely-known liposomal formulations for doxorubicin delivery, Doxil and Myocet, rely on design principles that do not translate to PTX. Because of

doxorubicin's chemical structure, it is more hydrophilic (logP = 1.3) than PTX (logP = 3.96) and can even be administered directly to patients without a solubilizing agent. Moreover, doxorubicin has functional groups that allow it to be loaded via pH or ion gradient loading methods (which PTX lacks) to form reversibly soluble crystals within the liposomal aqueous pocket[33]. Instead, PTX incorporates within the hydrophobic layer of lipid membranes to variable extents depending on the lipid composition[24,34–36]. PTX is typically soluble in lipid membranes on the order of one day or longer when loaded at or below 3 mol% of the total liposome formulation[24,34]. Once PTX phase separates into stable insoluble crystals, the bioavailability of the drug drops significantly[24,34,37–39]. Thus, it is critical to evaluate the duration of PTX solubility (an indicator of drug loading and retention) in new lipid formulations to ensure the drug remains soluble on relevant timescales for delivery[34].

Of the different types of lipid NPs, *cationic* liposome (CL) NPs were chosen for this study because positively charged particles have been shown to passively accumulate in tumors[30,40–44]. Tumor vasculature has a greater negative charge than other tissue[26,42], and thus positively charged particles adhere more to this area. Further, the CL_{PTX} NP formulation EndoTAG (aka SB05), owned by SynCore Biotechnology, has completed Phase II clinical trials[14,41]. EndoTAG is composed of the univalent cationic lipid 2,3-dioleyloxypropyltrimethylammonium chloride (DOTAP), neutral 1,2-dioleoyl-*sn*-glycero-3-phosphatidylcholine (DOPC), and PTX (50:47:3 mole ratio) and is used as a benchmark with which to compare the novel formulations presented here[27].

The current study was designed to elucidate the effects of PEGylating (PEG: polyethylene glycol) CL_{PTX} NPs on NP structure, morphology, and interactions with human cancer cells *in vitro*. This is useful knowledge to obtain because PEG is used to generate "stealth" NPs by delaying their detection and clearance by the immune system, thus increasing their circulation time[45,46]. However, addition of PEG-lipid to CL NPs is known to affect their self-assembly and other physical properties. The conformational transition from the mushroom to the brush regime of PEG decorating liposomes has previously been described as a function of PEG length and mol% composition[47,48]; for PEG2K-lipid, this transition occurs

between 5 and 10 mol%. The CL_{PTX} NPs studied here consisted of mixtures of DOTAP, DOPC, PTX, and a neutral PEG-lipid with two oleyl tails and a PEG molecular weight of 2,000 g/mol (PEG2K-lipid). NPs were prepared at 0, 30, 50, and 80 mol% DOTAP to detect any separate effects of membrane charge density on NP efficacy. Remarkably, cell viability studies show that PEGylating CL_{PTX} NPs by replacing a fraction of DOPC with PEG2K-lipid (5 and 10 mol%) dramatically enhances PTX delivery and cytotoxicity to human melanoma (M21) and prostate cancer (PC3) cells. This deviates significantly from the effect of PEGylation on the efficacy of CL-DNA NPs employed in gene delivery[49–51], where the PEG coat suppresses electrostatic adhesion to the cell surface and cell entry.

We used confocal microscopy, flow cytometry, and cryogenic TEM to uncover the key differences underlying the interactions of bare and PEG-CL_{PTX} NPs with cells that cause PEGylation to enhance PTX delivery. Cryo-TEM shows that adding PEG-lipid (5 and 10 mol% PEG2K-lipid) or charged lipid (30, 50 and 80 mol% DOTAP) to neutral DOPC vesicles induces a structural transition to a mixture of nanometer-scale vesicles and anisotropic micelles (primarily disc-shaped bicelles, Fig. 1). To our knowledge, the observed shape transition from vesicles to discoidal micelles, occurring at sub-monolayer PEG-lipid coverage, has not been reported previously. Notably, fluorescence confocal microscopy and flow cytometry reveal a major difference in CL_{PTX} NP interactions with the human cancer PC3 (prostate) and M21 (melanoma) cell lines depending on CL_{PTX} NP PEGylation. These studies show that PEG-CL_{PTX} NPs facilitate greater PTX delivery than bare CL_{PTX} NPs because, without a PEG coating, the latter form aggregates of NPs that adhere to the cell surface. Thus, the steric stability of NPs imparted by the PEG coat—which maintains their very small size by preventing NP-NP adhesion in cell medium—appears to be a critical factor that promotes cell uptake and PTX delivery through different size-dependent endocytic pathways[52], some of which, including endocytosis mediated by caveolae or clathrin, cannot transport large aggregates of bare NPs into the cell. (The *in vitro* experiments were performed in cell medium containing approximately 100 mM of 1:1 salts, which suppress the electrostatic repulsion between cationic NPs and facilitate clumping of bare NPs by van der Waals attraction.)

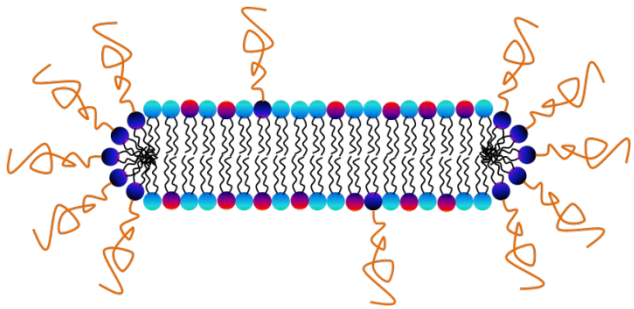

Figure 1. Schematic drawing of disk micelle. This figure depicts a cross section of a lipid disk micelle, also called a "bicelle". Disk micelles are formed by the addition of PEG-lipid to liposomes, which are typically bilayer vesicles. PEG-lipids (dark blue with orange projection) preferentially partition to the edge of the bilayer to relieve surface tension created by the bulky PEG headgroup, capping the bilayer edges to form disks.

The *in vitro* findings reported here are expected to have far-reaching implications for drug delivery *in vivo*, where size stability is a critical factor for cancer nanotherapy because it is thought that NPs on the order of 100 nm enter tumors through "leaky" vasculature. These small particles enter the tumor, but without a lymphatic drainage system, accumulate over time—the enhanced permeation and retention (EPR) effect—in another form of passive targeting[24,53]. The particles used in this study may be useful not only for drug delivery via systemic administration through blood, but also for intraperitoneal delivery[54], direct injection to tumors, *ex vivo* delivery, or *in vitro* cell-line experiments with difficult-delivery cell types. Furthermore, although not reported in the present work, a fraction of the pendant PEG moieties may be modified with targeting ligands to achieve active cell-specific targeting[24,55–57].

Experimental Section

Materials

Lipid stock solutions of DOPC and DOTAP in chloroform were purchased from Avanti Polar Lipids. PTX was purchased from Acros Organics and dissolved in chloroform at 10.0 mM concentration. Paclitaxel–OregonGreen® 488 conjugate (PTX_{GF}) and TRITC-DHPE ($lipid_{RF}$) were purchased from Thermo Fisher Scientific as powders and dissolved in chloroform to 190 μM and 81 μM concentrations, respectively. 1-((3,4-dioleyloxybenzoyl)oxy)-ω-methoxy-poly(ethylene glycol) 2000 (PEG2K-lipid) was synthesized in a manner analogous to that described for ω-hydroxy PEG-lipids[58] and dissolved in

chloroform to 10 mM. CellTiter 96® AQueous-One Solution Cell Proliferation Assay was obtained from Promega.

Liposome Preparation

Solutions of lipid and PTX were prepared in chloroform:methanol (3:1, v/v) in small glass vials at a total molar concentration (lipid + PTX) of 1 mM for cell viability experiments and DLS measurements, 5 mM for DIC microscopy, 400 μM for confocal fluorescence microscopy and flow cytometry, and 20 mM for cryoEM experiments. Individual stock solutions of each component were combined according to the final desired concentration and molar composition. The organic solvent was evaporated by a stream of nitrogen for 10 min and dried further in a vacuum (rotary vane pump) for 16 h. The resulting lipid/PTX films were hydrated with high-resistivity water (18.2 MΩ cm) to the previously described concentrations. Immediately thereafter, unless otherwise specified as "unsonicated", suspensions were agitated with a tip sonicator (Sonics and Materials Inc. Vibra Cell, set to 30 Watt output) for 7 min to form sonicated liposomes.

Cell culture

The human cell lines PC3 (ATCC number: CRL-1435; prostate cancer) and M21 (melanoma) were gifts from the Ruoslahti Lab (Burnham Institute, La Jolla). M21 cells are a subclone that was derived in the laboratory of Dr. Ralph Reisfeld (Scripps Institute, La Jolla) from the human melanoma line UCLA-SO-M21, which was originally provided by Dr. D. L. Morton (UCLA, Los Angeles). Cells were cultured in DMEM (Invitrogen) supplemented with 10% fetal bovine serum (Gibco) and 1% penicillin/streptomycin (Invitrogen). Cells were passaged every 72 h to maintain subconfluency and kept in an incubator at 37 °C in a humidified atmosphere containing 5% CO_2.

Cell viability experiments

This experiment was carried out as previously described[34]. Briefly, cells were plated in clear 96-well plates at a density of 5000 cells/well. Cells were incubated overnight to adhere to the plate. Sonicated

liposome suspensions were diluted in DMEM to reach the desired concentration of PTX. The cell culture medium was then manually removed from the wells and replaced with 100 μL of the liposome suspension. After incubation for 24 h, the liposome-containing medium was removed manually with a pipette and replaced with supplemented DMEM and returned to cell incubator. After another 48 h, the cell viability was measured with a 6X dilution of CellTiter 96® AQueous-One Solution Cell Proliferation Assay (Promega) in DMEM (120 μL of this solution were added to each well). The absorbance at 490 nm was measured with a plate reader (Tecan M220) after 1 h of incubation as per the assay instructions. Each data point is the average of four identically treated wells and reported as a percentage of the viability of untreated cells.

IC-50

The cell viability data for the IC_{50} determination was fit using the XLfit add-in for Microsoft Excel. The fit equation and fit parameters are reported in the Supplemental Information.

DIC microscopy for PTX solubility observation

Samples prepared at 5 mM concentration were either mixed manually after hydration by agitating the vial or tip sonicated, as specified. The sample solutions were stored at room temperature for the duration of the experiment. At predetermined times, 2 μL aliquots were withdrawn, placed on microscope slides, covered by a coverslip kept in place by vacuum grease, and imaged at 10 or 20 × magnification on an inverted Diaphot 300 (Nikon) microscope. The samples were first imaged within minutes of adding water to the dried lipid films, then every 2 h until 12 h, every 12 h until 72 h, and daily thereafter until PTX crystals were observed or the entire sample was used up. The kinetic phase diagrams report the median time to observation of PTX crystals after hydration for 3–4 independently formed samples at each mol% PTX.

Fluorescence microscopy

M21 and PC3 cells adhered to a 16 well plate were imaged with a microscope in fluorescence mode with a GFP filter using a 10x objective after a 5h incubation with bare or PEGylated CL NPs loaded with PTX_{GF}.

Confocal fluorescence microscopy

Particles were composed of DOTAP (30, 50, or 80 mol%) and PEG2k-lipid (0 or 10 mol%) as specified in the results section, 3 mol% PTX_{GF} conjugate, 0.2 mol% TRITC-DHPE, and the remainder DOPC. Particles were applied such that the PTX_{GF} concentration was 400 nM.

M21 and PC3 cells were seeded on poly-lysine coated coverslips in a 6 well plate at a concentration of 70,000 cells/mL, 2 mL/well. Twenty-four hours later, the cell media was removed and replaced with the solution of fluorescently-labeled particles. The cells were incubated for 5 hrs with the particles. After 5 hrs, the cells were fixed and microscope slides prepared.

Images were taken on Olympus DSU (spinning disk) confocal microscope with the disk in. The green and red fluorescence exposure time was 1 second.

Flow Cytometry

PC3 and M21 cells were plated in a 24-well plate at a concentration of 200,000 cells/mL with 500 μL of cell solution added to each well and allowed to adhere to the plate overnight. The following day CL NPs loaded with PTX_{GF} at 1 mol% were diluted in DMEM to a final concentration of $[PTX_{GF}] = 83$ nM. The cell media was removed from each well and replaced with 200 μL of CL NP solution. After a 5 hr incubation, the media was removed, cells were rinsed with PBS, trypsinized, and suspended in 200 mL DMEM. Fluorescence was measured using a Guava EasyCyte Plus Flow Cytometry System (Millipore). Cell solutions were passed through a 100 μm filter to disperse aggregates prior to measurement. The filtered cell solution was divided in two. One half was mixed with a Trypan Blue (Gibco) solution (0.4% in water, w/v) at a 4:1 (cell:Trypan Blue) v/v ratio and incubated for 10 min before the measurement to quench extracellular fluorescence. The other half of the cell solution was mixed with PBS at the same 4:1

v/v ratio and measured immediately. The software parameters were set such that 10 000 events constituted a single measurement. The flow cytometry results were analyzed using the Cyflogic software (CyFlo). Events were sorted using forward and side scattering to separate cells from debris. A single acceptance window was used for each sample. The green PTX_{GF} fluorescence distribution of the accepted events (cells) was log-normal, making the geometric mean (values reported in Fig. 5) a more accurate measure of the distribution than the arithmetic mean. The error bars show the uncertainty in the geometric mean which was calculated from the coefficient of variation (CV) of the fluorescence distribution using the following equation: $\sigma_{ERROR} = \log (CV^2–1) \times I/N$. Here, I is the geometric mean and N is the number of counted cells.

Cryo Electron Microscopy

All liposome samples were suspended in aqueous solution (high-resistivity water: 18.2 MΩ cm) and sonicated 24–36 h prior to vitrification. All samples were vitrified using a manual plunger on carbon lacey substrates (300 mesh copper grids) prepared in house (Fukami and Adachi, 1965). Grids were plasma cleaned using O_2 and H_2 for 30 s using a Solarus plasma cleaner (Gatan) immediately prior to sample preparation. 3 μL of sample was applied to the grid and manually blotted from the back with filter paper for 5 s followed immediately by plunging into liquid ethane. Images were acquired using Leginon (Suloway et al., 2005) on a Tecnai TF20 or Tecnai T12 equipped with 4K TVIPS CMOS camera, operated at 200 KeV or 120 KeV, respectively. Images were collected at nominal magnification of 62 kX (TF20) and 68 kX (T12), corresponding to pixel sizes of 3.0 Å/pixel and 2.46 Å/pixel, respectively. A summary of the image collection sessions is provided in Table S1 in the SI. The sample concentrations were typically 20 mM of total material (lipid + PTX) in high-resistivity water (18.2 MΩ cm).

Zeta potential

For zeta-potential measurements, liposomes were diluted to a lipid concentration of 100 μM in low salt 15 mM phosphate buffer saline solution. A 1 mL aliquot of the sample solution was loaded into a DLS

cuvette (Malvern DTS1070) and measured using a Malvern Zetasizer Nano ZS. The zeta-potential values are reported as the average ± standard deviation of 3 measurements.

Results

Incorporation of PEG2K-lipid to CL_{PTX} NPs increases efficacy

Following previous studies showing that PEGylating CLs decreases the delivery of nucleic acid[23,24,59], we tested to see if the same is true for PTX delivery by CLs—a physically and chemically distinct system. Two immortalized human cancer cell lines were treated with CL_{PTX} NPs. PC3 is a cell line derived from prostate cancer and overexpresses the neuropilin receptor, while M21 is derived from melanoma and does not express the neuropilin receptor. These cell lines were chosen for future testing of CLs that incorporate neuropilin-targeting ligands (not reported here), with M21 acting as the negative control for active targeting to the neuropilin receptor.

CL_{PTX} NPs with 0-14 mol% PEG2K-lipid were diluted in cell culture medium to a final PTX concentration of 60 nM (M21) and 50 nM (PC3) and added to cells (CL composition: 30 mol% DOTAP, 3 mol% PTX, 0-14 mol% PEG2K-lipid, and remaining mol% DOPC). Each cell line has a different dose-dependence on PTX, therefore they are treated with different PTX concentrations[34]. The resultant cell viability is reported in Figure 2a. Remarkably, for both M21 and PC3, the cell viability decreases as PEG2K-lipid is added into the formulation up to 10 mol%, then plateaus for PEG2K-lipid ≥ 10 mol%. At the PTX concentration tested, most cells remain alive after treatment with bare CL_{PTX} NPs, whereas the PEG-CL_{PTX} NPs kill the majority of cells with only about 20% of cells remaining viable after treatment.

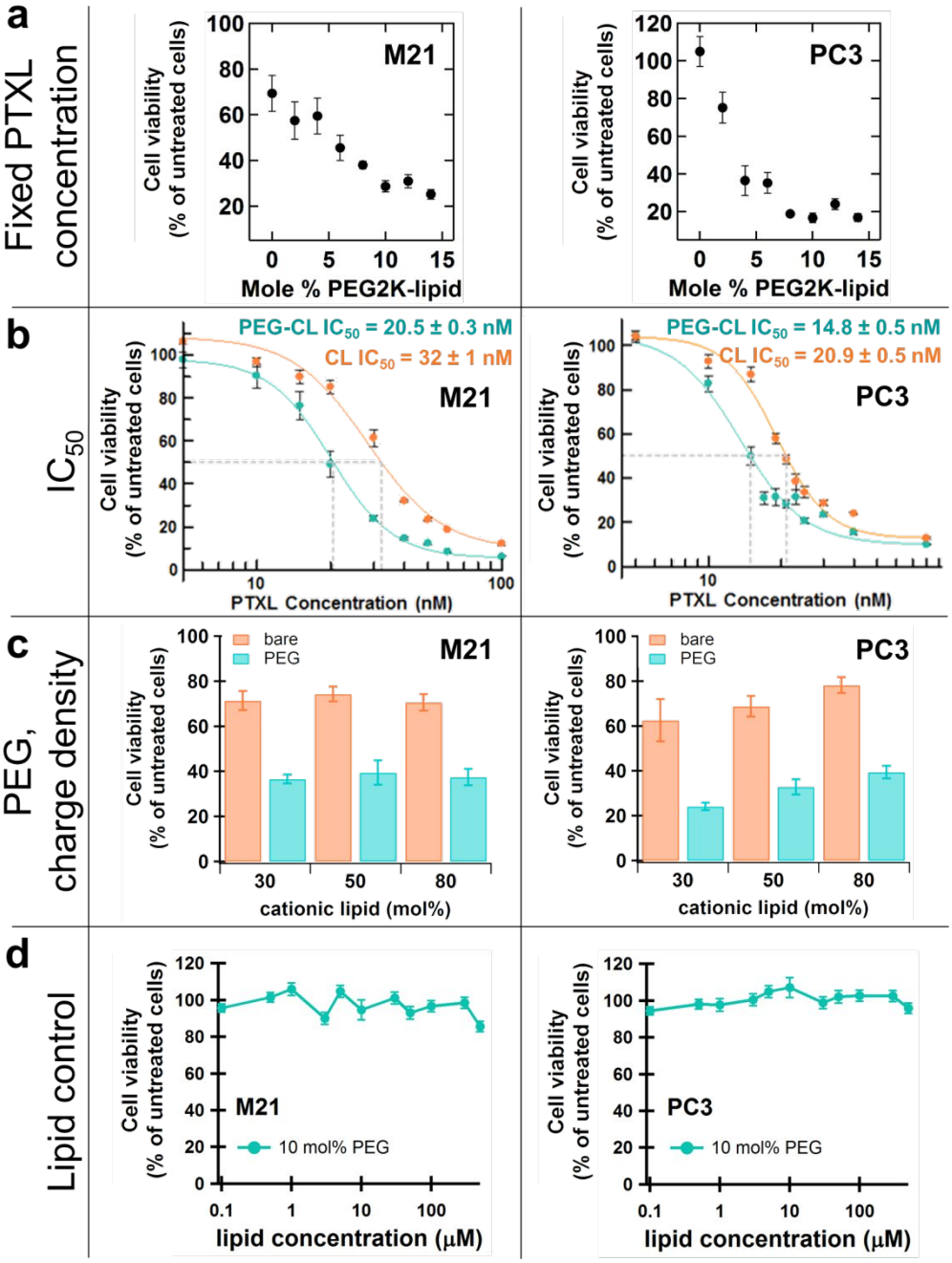

Figure 2: Cell viability of M21 and PC3 cells after treatment with bare and PEGylated CL_{PTX} NPs. (a) Cell viability after treatment with CL_{PTX} NPs of varied PEG2K-lipid content (0-14 mol%) at a fixed PTX dose for each cell line (M21 = 60 nM, PC3 = 50 nM); CL composition: PEG2K-lipid, DOTAP, DOPC, PTX (x_{PEG}:30:67-x_{PEG}:3 mol%). (b) IC_{50} determination of bare and 10 mol% PEG-CL_{PTX} NPs; CL composition: PEG2K-lipid, DOTAP, DOPC, PTX (x_{PEG}:50:47-x_{PEG}:3 mol%). (c) Cell viability after treatment with bare and PEGylated CL_{PTX} NPs of varied membrane charge density at a fixed PTX dose for each cell line (M21 = 50nM, PC3 = 40 nM); CL composition: 0/10 mol% PEG2K-lipid, 30/50/80 mol% DOTAP, 3 mol% PTX, 97-x_{PEG}-x_{DOTAP} mol% DOPC. (d) Control experiment assessing toxicity of PEGylated CLs without PTX over a range of lipid concentrations; CL composition: PEG2K-lipid, DOTAP, DOPC (10:50:40 mol%).

In a second experiment, CL_{PTX} NPs with either 0 or 10 mol% PEG2K-lipid were tested over a range of concentrations around the IC_{50} value. Here, the IC_{50} value is defined as the drug concentration at which cell viability is reduced by half the maximal theoretical response, i.e. when cell viability = 50%. The CL composition used in this experiment was 50 mol% DOTAP, 3 mol% PTX, 0 or 10 mol% PEG2K-lipid, and remaining mol% DOPC. The results in Figure 2b show that for M21, the IC_{50} of PEG-CL_{PTX} NPs is 20.5 ± 0.3 nM PTX compared to 32 ± 1 nM PTX of bare CL_{PTX} NPs ($p < 0.001$). Similarly, for PC3, the IC_{50} of PEG-CL_{PTX} NPs is 14.8 ± 0.5 nM compared to 20.9 ± 0.5 nM PTX of bare CL_{PTX} NPs ($p < 0.001$). See Figure S1 in the Supplemental Information (SI) for additional information on IC_{50} fitting parameters. The lower IC_{50} values show that PEGylated CL_{PTX} NPs achieve equivalent cell death outcomes using 25-33% less PTX than bare CL_{PTX} NPs.

In a third experiment, we determined the effects of cationic charge density on PTX delivery because charge is known to govern the efficacy of nucleic acid delivery by CL-based NPs. Here, cells were treated with six different CL_{PTX} NP formulations composed of 30, 50 or 80 mol% cationic DOTAP, with and without 10 mol% PEG2K-lipid (PTX = 3 mol%; remaining mol% DOPC). The results in Figure 2c show that cell viability is significantly lower for the PEGylated CL_{PTX} NPs compared to the bare CL_{PTX} NPs at each charge density for both M21 and PC3 cells ($p < 0.001$ for all except PC3 at 30 mol% DOTAP which has $p < 0.01$). Cell viability of M21 cells after treatment with bare and PEGylated CL_{PTX} NPs was approximately 70% and 40%, respectively, regardless of the CL charge density. Similarly, for PC3 cells, the PEGylated CL_{PTX} NPs yielded cell viabilities lower 40 percentage points than the bare CLs at each charge density. Efficacy in PC3 cells appears to have a slight dependence on charge density, with cell viability increasing as cationic DOTAP increases from 30 to 80 mol%.

The results of a control experiment to ensure there is no innate toxicity of PEG-CL NPs are shown in Figure 2d. M21 and PC3 cells were treated with PEGylated CLs without PTX over a broad range of concentrations. No toxicity was observed over the tested range of CLs (0.1-500 μM lipid) incorporating 10 mol% PEG2K-lipid. For reference, when cells are treated with PTX at concentrations of

10-100 nM and PTX is 3 mol% of the liposome composition, the total lipid concentration is 0.3-3 μM, well within the observed non-toxic range. This control experiment demonstrates that the increased toxicity of PEG-CL_{PTX} NPs must be the result of how the incorporation of PEG-lipid alters the physicochemical properties of the CL vector to alter the PTX delivery mechanism and enhance efficacy.

Fluorescent imaging and flow cytometry show that PEGylation enhances CL_{PTX} NP uptake in cells

Figure 3 shows fluorescent microscope images (taken on a DIC microscope in fluorescence mode) of cells treated with CL NPs loaded with green fluorescent PTX (PTX_{GF}) at low magnification. The PTX_{GF} (OregonGreen® 488–PTX), as previously described[34], is somewhat more soluble in water than unmodified PTX; however, it still retains its binding affinity to tubulin and is hydrophobic such that it preferentially partitions into lipid membranes. Therefore, it is expected to be an accurate qualitative indicator of the activity of unmodified PTX. PTX_{GF} (ThermoFisher reports a typical working concentration for live cell microtubule imaging is 1 μM and that no toxicity to HeLa cells is observed at 1 μM) is less cytotoxic than unmodified PTX (typical working concentration is 0.1 μM); at the PTX_{GF} concentrations used in our experiments (400 nM and 83 nM for fluorescence microscopy and flow cytometry, respectively) we do not expect that PTX_{GF} has significant cytotoxic impacts during imaging and flow cytometry that could obscure the results.

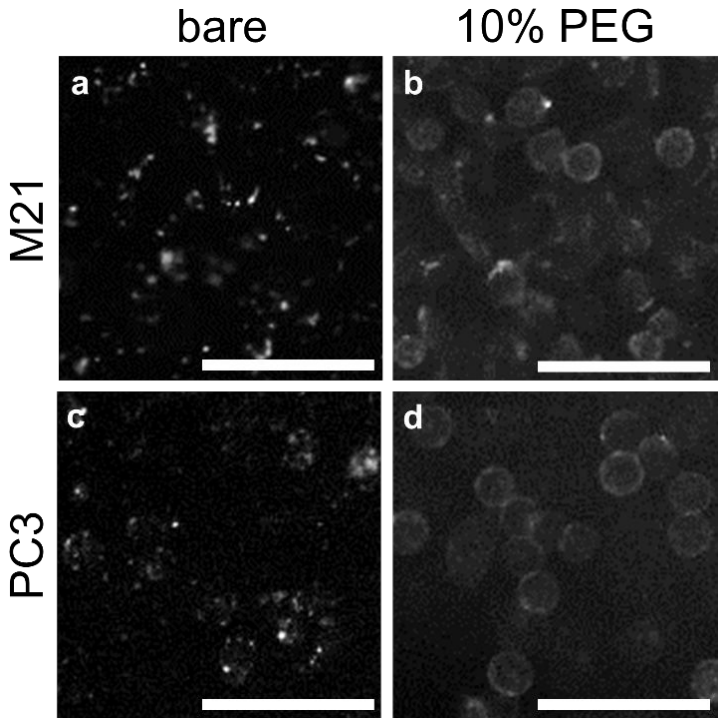

Figure 3: Fluorescent microscope images of M21 and PC3 cells in medium treated with bare and PEGylated CL_{PTX} NPs. M21 (a,b) and PC3 (c,d) cells were incubated with either bare (a,c) or PEGylated (b,d) CLNPs fluorescently labeled by PTX_{GF} for 5 h. CL composition: PEG2K-lipid (0/10 mol%), DOTAP (30 mol%), PTX_{GF} (3 mol%), and DOPC (remaining mol%). Scale bars are 100 μm.

PEGylation of CL_{PTX} NPs induces major differences in the PTX_{GF} association with cells. The fluorescence from bare CL_{PTX} NPs (Figs. 3a,c) appears as brighter concentrated spots around the cell periphery, suggesting that there are clumps of NPs bound to the cell surface. In contrast, the PTX_{GF} fluorescence from PEG-CL_{PTX} NPs (Figs. 3b,d) illuminates the cells and is more diffuse and distributed across cells (indicative of PTX delivery), though brighter at the cell perimeter. The original uncropped images as well as images from repeated experiments are shown in Fig. S2 of the Supporting Information. The top-down fluorescence imaging on the DIC microscope yields images showing the total fluorescence throughout the full height of the cells.

Using red fluorescent lipid ($lipid_{RF}$) and PTX_{GF} further reveals differences in the lipid and PTX distributions after delivery from bare CL_{PTX} NPs compared to PEG-CL_{PTX} NPs. Figure 4 displays confocal fluorescent microscopy results (showing cross-sectional slices at defined heights within the cells) for CL_{PTX} NPs of different charge density, with and without 10 mol% PEG2K-lipid on both the M21 (a-f) and PC3 (g-l) cell lines; additional confocal images and analysis are provided in Figures S3-5 in the SI. Cell outlines are drawn in yellow from brightfield images (Fig. S3) at the plane where the cell is

adhered to the coverslip (z = 0). The height above this plane at which the fluorescence was recorded is reported on each image in white font as z_{fluor}.

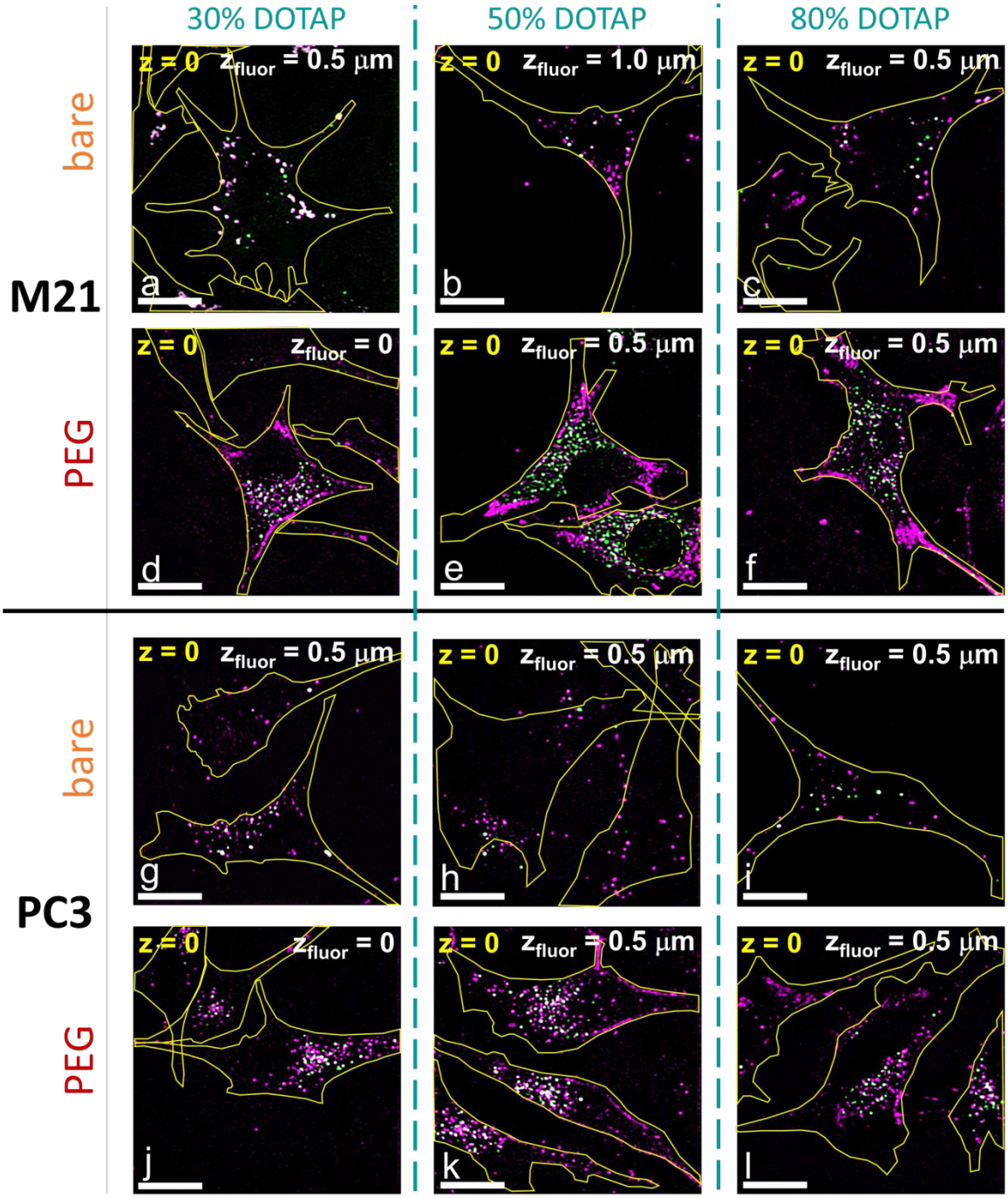

Figure 4: Fluorescent confocal microscopy of bare and PEGylated CL_{PTX} NPs incubated with M21 and PC3 cells in medium. M21 (a-f) and PC3 (g-l) cells were incubated with CLNPs of different charge density and PEGylation, fluorescently labeled by $lipid_{RF}$ (magenta) and PTX_{GF} (green). Solid yellow lines show cell outlines estimated from brightfield images at the plane adhered to the glass coverslip (z = 0)

(see Supporting Information); z_{fluor} in white indicates the distance above z = 0 that the fluorescent image corresponds to. The nuclear region in (e) is indicated by the yellow dashed line. CL composition: PEG2K-lipid (0/10 mol%), DOTAP (30/50/80 mol%), PTX_{GF} (3 mol%), TRITC-DHPE (0.2 mol%), and DOPC (remaining mol%). Scale bars are 20 μm.

Several distinct features are observed in the array of images shown in Fig. 4. For both M21 and PC3 cells, the appearance of the fluorescence changes dramatically between the bare CL_{PTX} NPs (a-c, g-i) and the PEG-CL_{PTX} NPs (d-f, j-l) at each charge density. Bare CL_{PTX} NPs typically appear as fewer, often larger and brighter spots than PEG-CL_{PTX} NPs. Much of the fluorescence from bare CL_{PTX} NPs is visible toward the outer edge of the cells, likely adhering to the outside of the cells, with significantly less material entering the cells compared to the PEG-CL_{PTX} NPs.

It is evident that more PEG-CL_{PTX} NP material entered cells based on the greater number of punctate fluorescent spots distributed throughout the cell interiors, excluding the nucleus. Nuclei were not stained in this experiment, however the distribution of particles within the cells, particularly in Fig. 4e, strongly suggests that the lipid (magenta) and PTX (green) remained outside the intact nucleus (see the yellow dashed circle). Figure S4 provides several series of z-slices that further demonstrate the differences between PEG-CL_{PTX} NPs and CL_{PTX} NP uptake from the bottom to the top of cells.

Comparing the images of M21 and PC3 cells treated with PEG-CL_{PTX} NPs, the $lipid_{RF}$ and PTX_{GF} appear to be more segregated in M21 cells. The $lipid_{RF}$ (magenta) partitions more diffusely toward the cell perimeter, whereas the PTX_{GF} (green) persists as spots in the interior. In PC3 cells treated by PEG-CL_{PTX} NPs, the $lipid_{RF}$ appears more punctate within the cell and more colocalized (white) with PTX_{GF}, though the $lipid_{RF}$ has concentrated in several areas at the PC3 cell membrane edges. The differences in colocalization are shown more quantitatively in Fig. S5, which provides selected line scans corresponding to fluorescence variation of each fluorophore.

The results of flow cytometry experiments reported in Fig. 5 provide a statistical measure of the PTX_{GF} fluorescence associated with cells after delivery by CL_{PTX} NPs with 0, 5 or 10 mol% PEG2K-lipid (CL compositions: 30 mol% DOTAP, 0/5/10 mol% PEG2K-lipid, 1 mol% PTX_{GF}, and the remainder

DOPC). CL_{PTX} NPs were incubated on cells for 5 hrs, after which the green fluorescence of half of the CL-treated cells was measured directly by flow cytometry to determine the total PTX_{GF} associated with cells (adhesion plus uptake). The other half of the CL-treated cells were incubated with Trypan Blue dye for 10 minutes before the fluorescence was measured. Trypan Blue quenches the fluorescence on the outside of the cells, thus yielding the amount of internalized PTX_{GF} (uptake). Histograms showing the PTX_{GF} fluorescence intensity distribution of cells after CL NP incubation and after Trypan Blue quenching are shown in Fig. S6 of the Supporting Information. For PC3 and M21 cells, both the total amount of PTX_{GF} associated with the cell (equal to the full height of the bar: adhesion plus uptake) and the amount of internalized PTX_{GF} (uptake, lower green bar only) increases as the mol% of PEG2K-lipid increases. Moreover, the fraction of internalized PTX_{GF} out of total PTX_{GF} (reported as percentage on bar) is greater for PEGylated CL_{PTX} NPs. Similar flow cytometry experiments were performed to determine the effect of charge density. The trends as a function of charge density appear to be cell line dependent. This data is provided in Fig. S7. These results agree with the data reported in Fig. 5 wherein both PTX_{GF} adhesion and uptake are consistently enhanced by PEGylation.

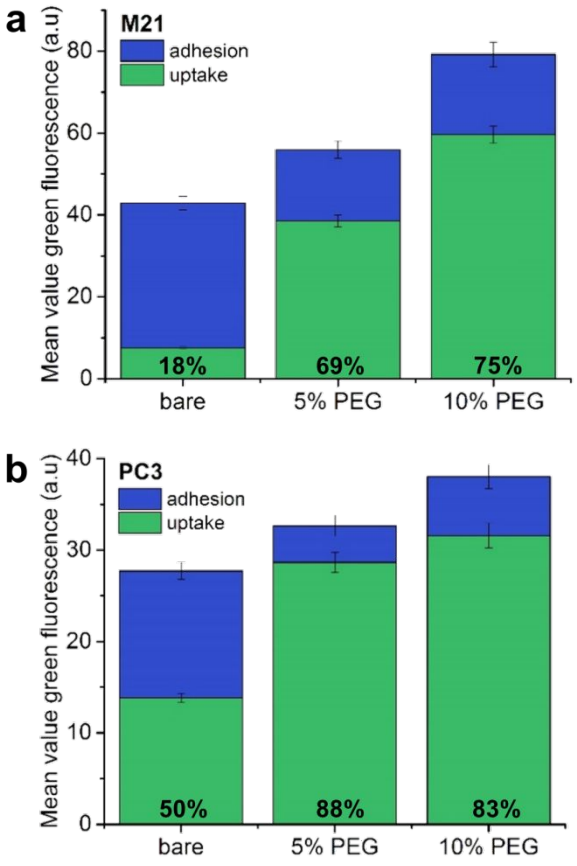

Figure 5: Flow cytometry measurement of PTX_{GF} uptake after delivery from bare or PEGylated CL_{PTX} NPs. CL_{PTX} NPs loaded with 1 mol% PTX_{GF} and 0, 5, or 10 mol% PEG-lipid were incubated with (a) M21 and (b) PC3 cells in medium for 5 h before measuring the cell-associated PTX_{GF} by flow cytometry. First, the total PTX_{GF} fluorescence associated with cells was measured and is reported as the total height of the bar (adhesion + uptake). Second, the same measurement was performed after quenching the fluorescence on the outside of cells with Trypan Blue dye to yield the amount of PTX_{GF} that was inside of cells (uptake). The fraction of PTX_{GF} that was taken up by cells with respect to the total amount of PTX_{GF} associated with cells is reported as a percentage on each bar. CL composition: PEG2K-lipid (0/5/10 mol%), DOTAP (30 mol%), PTX_{GF} (1 mol%), and DOPC (remaining mol%).

PEGylation decreases PTX solubility in lipid membranes

We have shown that PTX membrane solubility affects CL_{PTX} NP efficacy[34]. Therefore, we assessed the effect of PEGylation on the solubility of PTX in CL membranes at room temperature over time. Due to the hydrophobic nature of PTX and its propensity to form stable crystals in aqueous solution, the appearance of PTX crystals indicates PTX release from liposomes[34,37]. Figure 6 displays DIC microscopy images and kinetic phase diagrams generated from those images which show that PEGylation slightly decreases PTX solubility in CL_{PTX} NPs. Data is shown for both unsonicated (Fig. 6a) and sonicated (Fig. 6b) CL_{PTX} NPs. The colored blocks in the phase diagrams indicate the solubility front for PEG-CL_{PTX} NPs, whereas the black line demarcates the solubility front for the corresponding bare CL_{PTX} NPs. Consistent with the decreased duration of solubility, PTX crystals formed from PEG-CLs were

typically shorter, thinner and more numerous than those originating from bare CLs, indicating that more nucleation sites occurred in the PEG-CLs (see Fig. 6c).

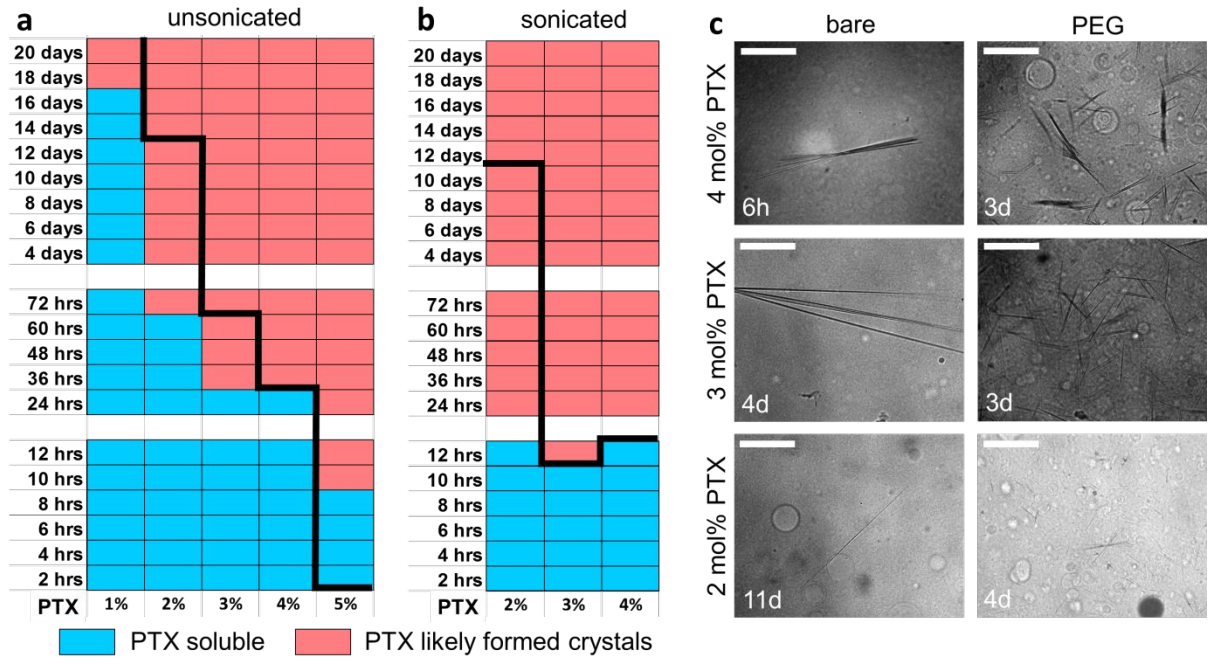

Figure 6: PTX solubility in lipid membranes as a function of sonication, PEGylation and drug loading. Kinetic phase diagrams indicate the duration of PTX solubility in (a) unsonicated and (b) sonicated liposomes after lipid film hydration. Blue indicates PTX solubility in PEGylated membranes; pink indicates when PTX is likely to have phase separated. PEGylated CL composition: PEG2K-lipid, DOTAP, DOPC, PTX (10:50:40-x_{PTX}:x_{PTX} mol%). The black reference line indicates the solubility boundary for bare liposomes (no PEG); bare CL composition: DOTAP, DOPC, PTX (50:50-x_{PTX}:x_{PTX} mol%). (c) DIC microscopy images of PTX crystals from unsonicated bare and PEGylated liposomes, loaded with 2-4 mol% PTX; the time since lipid hydration is indicated on the images. Scale bars are 100 μm.

Cryogenic TEM reveals different vesicle and micelle structures as a function of CL_{PTX} NP composition

We used cryogenic TEM (cryo-TEM) to evaluate the structures of particles as a function of liposome composition. The solvent in all the samples is deionized water and all samples were sonicated 24–36 h prior to vitrification. The images reveal a significant morphological dependence on both charge

density and PEGylation. We compared neutral liposomes (0 mol% DOTAP, 97 mol% DOPC, 3 mol% PTX) to DOTAP/DOPC CLs containing 50 or 80 mol% DOTAP, bare or with 10 mol% PEG2K-lipid.

The bare neutral liposomes appear to be in a pure bilayer phase (Fig. 7a white arrows); there is no indication of micelles. The incorporation of 10 mol% PEG2K-lipid to the neutral liposomes induces the formation of discoidal micelles (Fig. 7d and enlarged box in 7g). The disk shape is identified primarily by the appearance of elliptical shapes (green solid arrows), which correspond to disks tilted at an angle between parallel and perpendicular to the imaging plane. When the disks are at a full 90° (perpendicular) tilt, they appear to be dark rods (green arrowheads). When the disks are parallel to the imaging plane, they appear to be faint circles (dashed green arrows) whose appearance is markedly different from that of vesicles. Vesicles (white arrows) have dark outlines, reflecting the higher electron density at the edge of a sphere projected on two dimensions. Discoidal micelles, also known as “bicelles” (Fig. 1), have a more uniform electron density across the face of the micelle, with perhaps some crowding at the edge where the hydrophobic layer is capped. The PEGylated neutral liposomes exhibit a coexistence of vesicles and disc micelles.

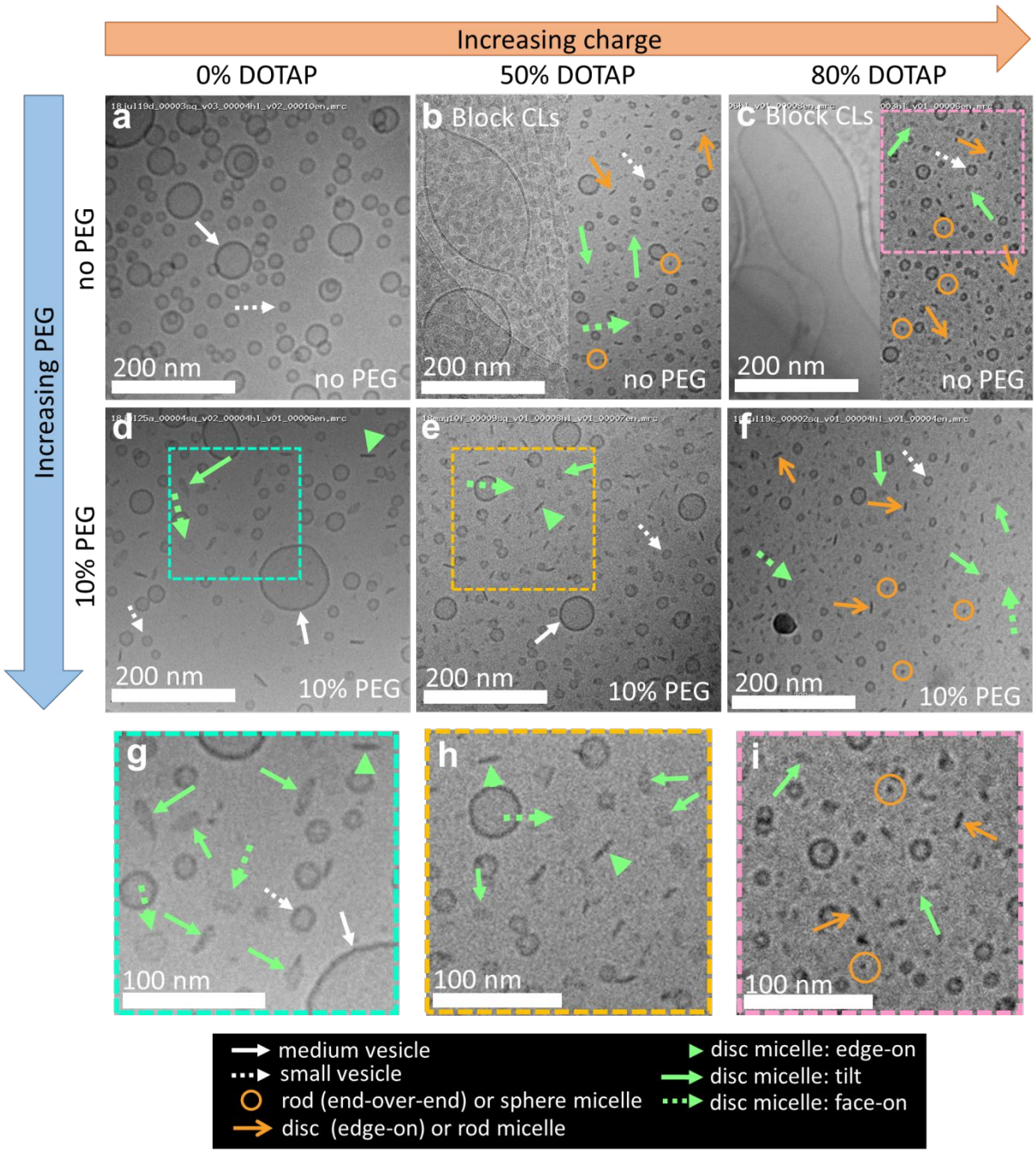

Figure 7: CryoTEM micrographs show the effects of PEGylation and membrane charge density on NP morphology. In (a) neutral uncharged membranes (0 mol% DOTAP) without PEG-lipid form bilayer vesicles (white arrows). As PEG-lipid and/or charged lipids (b-f) are incorporated into the liposome formulations, the average vesicle size decreases and disc- (green arrowheads, solid and dashed arrows indicate different disc tilts), rod- (orange arrows) and sphere-shaped (orange circles) micelles emerge. Larger views of the dashed boxes in (d), (e), and (c) are shown in (g), (h), and (i), respectively. See text for more information regarding the micelle shapes.

The introduction of univalent cationic lipid to bare neutral lipid decreases the median vesicle size (see supplemental Fig. S8) and simultaneously leads to the formation of giant tubular vesicles reminiscent of "block liposomes", which are giant liposomes that have distinct tubular and spherical shaped sections (labeled "Block CLs" in the split panels in Figs. 7b-c)[60–62]. Cationic lipid appears to also induce the formation of very small discoidal (green arrows), rod, or spherical micelles (orange arrows and circles) as indicated in Figure 7. It is difficult to distinguish the three-dimensional forms of the micelles based on the two-dimensional EM images (Fig. 7i). What appear to be rods in 2D (orange arrows), may be either discs edge-on to the imaging plane or actual rods. Similarly, the very small dots (orange circles) may be spherical micelles or rods tilted end-over-end. Overall, the bare charged membranes contain a mixture of block liposomes, vesicles, and micelles.

Importantly, when PEG is added to charged membranes (Figs. 7e-f), it eliminates the giant tubular liposomes observed in the bare (50 and 80 mol% DOTAP) CL formulations. Disk micelles dominate in the PEGylated sample at 50 mol% DOTAP (Fig. 7e); however, as the charge increases further to 80 mol% DOTAP (Fig. 7f), rods and/or spheres become more abundant. Median vesicle and micelle diameters are reported in the SI (Fig. S8). Vesicle size of bare liposomes decreases as a function of increasing charge from 21 nm diameter at no charge to 12 nm at 80 mol% DOTAP. There was no significant size difference between PEGylated vesicles of 50 and 80 mol% DOTAP (16 nm) following a median size decrease of about 3 nm from no charge (19 nm) to 50 mol% DOTAP. The micellar objects in the bare samples with 50 and 80 mol% DOTAP had median lengths of 8 nm. Conversely, the micelles in the PEGylated samples continue to decrease in diameter as a function of increasing charge, from a disc diameter of 20 nm at neutral charge to 11 nm at 50 mol% DOTAP and 8 nm at 80 mol% DOTAP, which reflects the appearance of smaller micellar rods and/or spheres. In bare liposomes, no micelles form without cationic lipid, while greater than half the objects observed in EM are micelles at or above 50 mol% DOTAP. The number fraction of micelles increases from 0.4 to over 0.7 as the charge of the PEGylated liposomes increases (Fig. S8). Figure S8 also shows the z-averages measured by DLS of CL

NPs with 0, 5, and 10 mol% PEG2K-lipid at 30, 50, and 80 mol% DOTAP; however, the DLS technique is not equipped to yield an accurate measure of the complex, polydisperse CL NP samples reported here. Phase separated PTX had a conspicuous appearance in cryo-TEM images, forming 100–200 nm thick needle-like crystals with persistence lengths much larger than the imaging frame (shown in Fig. S9).

Discussion

The cell viability, fluorescence microscopy and flow cytometry results indicate a significant enhancement of PTX delivery and cytotoxicity to cells *in vitro* as a result of PEGylating CL_{PTX} NPs. Rather than diminishing drug delivery, PEG enhances PTX uptake by cells. This result is surprising because in other cationic NP delivery systems (such as CL-nucleic acid NPs), PEGylation hinders particle-cell interactions by blocking attractive electrostatic forces and decreases delivery of the therapeutic cargo compared to bare cationic vectors[49–51]. Zeta potential measurements (Supplemental Fig. S10), measured in low salt solution (15 mM PBS), demonstrate the expected decrease of particle surface charge with increasing PEGylation at 5 and 10 mol%, but show that a net positive charge remains.

The IC_{50} dose-response curves (Fig. 2b) reveal that 25-33% less PTX drug was needed from PEG-CL_{PTX} NPs than bare CL_{PTX} NPs to reach equivalent cell death outcomes. When we observed how particles interacted with cells after short CL_{PTX} NP incubations (5 hrs) using fluorescent confocal microscopy and flow cytometry, the differences between the bare and PEGylated CL_{PTX} NPs were both qualitatively and quantitatively apparent. Fluorescence confocal microscopy showed that PEGylated CLs enhanced particle internalization in both M21 (human melanoma) (Fig. 4d-f) and PC3 (human prostate) (Fig. 4j-l) cell lines. In addition to colocalization of $lipid_{RF}$ (magenta) and PTX_{GF} (green) (i.e. white intact NPs), these images indicated distinct spatial segregation of the $lipid_{RF}$ and PTX_{GF} after delivery by PEG-CLs; this effect was especially pronounced in M21 cells. Here, $lipid_{RF}$ may have fused with the cell membrane, as evidenced by the diffuse fluorescence concentrated toward the outer cell periphery.

Importantly, there was a significant amount of PTX_{GF} within the cells treated with PEGylated CLs, largely concentrated in punctate spots in the cytoplasm, and excluded from the nucleus (see yellow dashed region in Fig. 4e), which suggests it was confined within endocytic compartments. In contrast, particle incubation with bare CLs (Figs. 4a-c,g-i) yielded significantly fewer but often times brighter spots of fluorescence, either adhered to or within cells. These fluorescent nodes frequently contained colocalized $lipid_{RF}$ and PTX_{GF} (white) (Fig. 4a).

Flow cytometry (Fig. 5) showed increasing total PTX_{GF} associated with cells (adhesion plus uptake is equal to the total bar height) and higher uptake (green bar) as PEG2K-lipid was incorporated into particles from 0 up to 10 mol%. This suggests that the reason for greater cell-death response and lower IC-50 values is that more drug is shuttled into the cells and internalized from the PEGylated CL_{PTX} formulations. Furthermore, these experiments indicated that a large amount of PTX_{GF} delivered by bare CLs adhered to the outside of cells but was not internalized at the 5 h time point. We can surmise this based on the low percentage of cell-associated PTX_{GF} that was internalized from bare CLs. This is consistent with the fluorescence patterns observed in confocal microscopy that also indicated bare CLs adhered to cells but were internalized to a much lesser extent than PEG-CLs.

In addition to PEGylation, we explored the effects of varying the CL cationic charge density on PTX delivery. The cell viability experiment in Figure 2c (24 h CL incubation) did not show a dependence on CL charge density for M21 cells. In contrast, PC3 cells exhibited a small charge density dependence, with lower charge density CLs (30 mol% DOTAP) causing greater cell death than higher charge density CLs (80 mol% DOTAP), for both bare and PEGylated CLs. Interestingly, in confocal microscopy (5 h CL incubation), a qualitative difference appeared in the fluorescence patterns of CL-treated cells wherein the $lipid_{RF}$ and PTX_{GF} colocalization was more pronounced for bare CLs at 30 mol% DOTAP than at 50 or 80 mol% DOTAP.

Flow cytometry results for bare and PEGylated CLs at 30, 50 and 80 mol% DOTAP are included in the Supplemental Information (Fig. S7). These results were consistent with the results in Fig. 5 (a

separate experiment using 30 mol% DOTAP CLs) and indicate that PEGylation enhances PTX_{GF} uptake at all charge densities tested. However, the results vary as a function of charge density by cell line. Cationic charge is at best secondary to PEGylation as a contributing factor to PTX delivery *in vitro*, and its importance is cell line dependent. However, based on our understanding of passive electrostatic targeting mechanisms in systemic delivery systems, it would be important to test CL_{PTX} NP charge density in *in vivo* studies, which could reveal an environmental dependence on charge.

As previously described[34], the more soluble PTX is in its delivery vector, the greater its efficacy. As reported in the kinetic phase diagrams in Fig. 6, the inclusion of PEG2K-lipid somewhat shortens the time PTX is soluble in lipid membranes (i.e. drug retention). This finding is consistent with a report from Crosasso et al.[63] on the solubility of PTX in negatively charged bare and PEGylated liposomes determined by HPLC methods. That PEGylation decreases PTX solubility suggests that, if anything, it would also decrease PTX delivery. Therefore, there must be a separate mechanism to explain the delivery enhancement. It is worth noting that in the cell viability experiments reported in Fig. 2, PTX was loaded at 3 mol% and CLs were prepared just before incubation with cells. At this drug loading, the PEGylated and bare CL_{PTX} NPs exhibit similar PTX solubility, phase separating by 12 h.

We next turned to cryo-TEM (Fig. 7) to investigate whether the morphological properties of the CL NPs could account for the variation in PTX delivery efficacy. A detailed explanation of distinguishing vesicles, block liposomes, and disk, rod or sphere-shaped micelles is given in the results section; NP size analysis is reported in Fig. S8 in the SI. In the extreme case of uncharged membranes (0 mol% DOTAP) without PEG2K-lipid (Fig. 7a), we observe only bilayer vesicles (white arrows) in a distribution of sizes. The median vesicle diameter of 21 nm is unexpectedly small for uncharged LNPs. The incorporation of PEG2K-lipid to neutral membranes induced the formation of discoidal micelles with 20 nm diameter (Fig. 7d,g).

The steric bulk of PEG extending from the lipid headgroup creates a surface tension that is relieved when a NP assumes a disc morphology; this occurs by preferential partitioning of the cone-

shaped PEG2K-lipids (due to their large positive spontaneous curvature) to the disc's edge which lowers the membrane curvature elastic energy (see Fig. 1)[64–68]. Discs persist throughout the PEGylated samples, but coexist with rods and/or spheres at higher charge density. Due to the projection of 3D objects on a 2D plane, it is difficult to determine to what extent these objects coexist. Charged lipids, similar to PEG-lipids, are cone-shaped and have a positive spontaneous curvature, and therefore favor forming small vesicles and micelles with higher curvature. High charge, also like PEG, prevents NP coalescence through repulsive electrostatic forces between discrete CL NPs; however, this stabilizing effect is lessened in salt solution, such as cell culture medium, by charge screening.

The important remaining question is by what mechanism(s) PTX is actually delivered to cells. Confocal microscopy revealed that bare CL_{PTX} NPs formed micron-scale clumps adhered to the cell surface (i.e. brighter fluorescent spots observed in Figs. 4a-c,g-i). This was most likely due to van der Waals attraction between NPs where the electrostatic repulsion between cationic NPs was strongly suppressed in cell medium with ≈ 100 mM of 1:1 salts. (The cryo-TEM samples were prepared in deionized water, so the bare CL_{PTX} NPs were charge-stabilized.) The large aggregates of bare NPs adhered to the outside of cells (as evidenced in flow cytometry by the drop in cell-associated PTX_{GF} after quenching external green fluorescence (Fig. 5)) strongly suggest there is a size barrier to cell entry by endocytosis. In striking contrast, confocal images and flow cytometry revealed a distinct enhancement of PEG-CL_{PTX} NP uptake into cells.

Taken together, the data suggest a model where the steric stability of PEG-CL_{PTX} NPs— in which NP-NP aggregation due to van der Waals interactions is suppressed, independent of the salinity conditions, by the repulsive forces of the PEG coat—is a critical factor in facilitating cell uptake and PTX delivery by different size-dependent endocytic pathways[52].

Although fluorescence microscopy and flow cytometry show low PTX_{GF} uptake from bare CL_{PTX} NPs (Figs. 3-5) after a short incubation (5 h), the cell viability measurements (Fig. 2) demonstrate that over longer incubation periods (24 h), PTX from bare CL_{PTX} NPs does cause cell death, albeit at a higher

dose of PTX. Due to the low uptake of bare CL_{PTX} NPs observed in microscopy and flow cytometry at the 5 h time point, it is likely that PTX continues to transfer from CL to cell membrane over time, aided by electrostatic adhesion of the particles to the cell membrane.

Since PTX is a hydrophobic molecule, we expect that it can transfer between lipid sinks (from CL_{PTX} NP to membrane to membrane) during collisions to reach its tubulin target, without the need for an active release mechanism to achieve drug delivery. This model is illustrated in Figure 8. This would explain why PEGylation does not have an adverse effect on CL_{PTX} NP delivery as it does in other drug delivery systems where it blocks membrane-membrane interactions essential to cell uptake and endosomal escape. The smaller, sterically stabilized, PEGylated CLs are taken up by cells via endocytosis on shorter time scales and in greater number than bare CL_{PTX} NPs. This brings the PTX drug inside of the cell, fewer steps away from its target, and facilitates delivery.

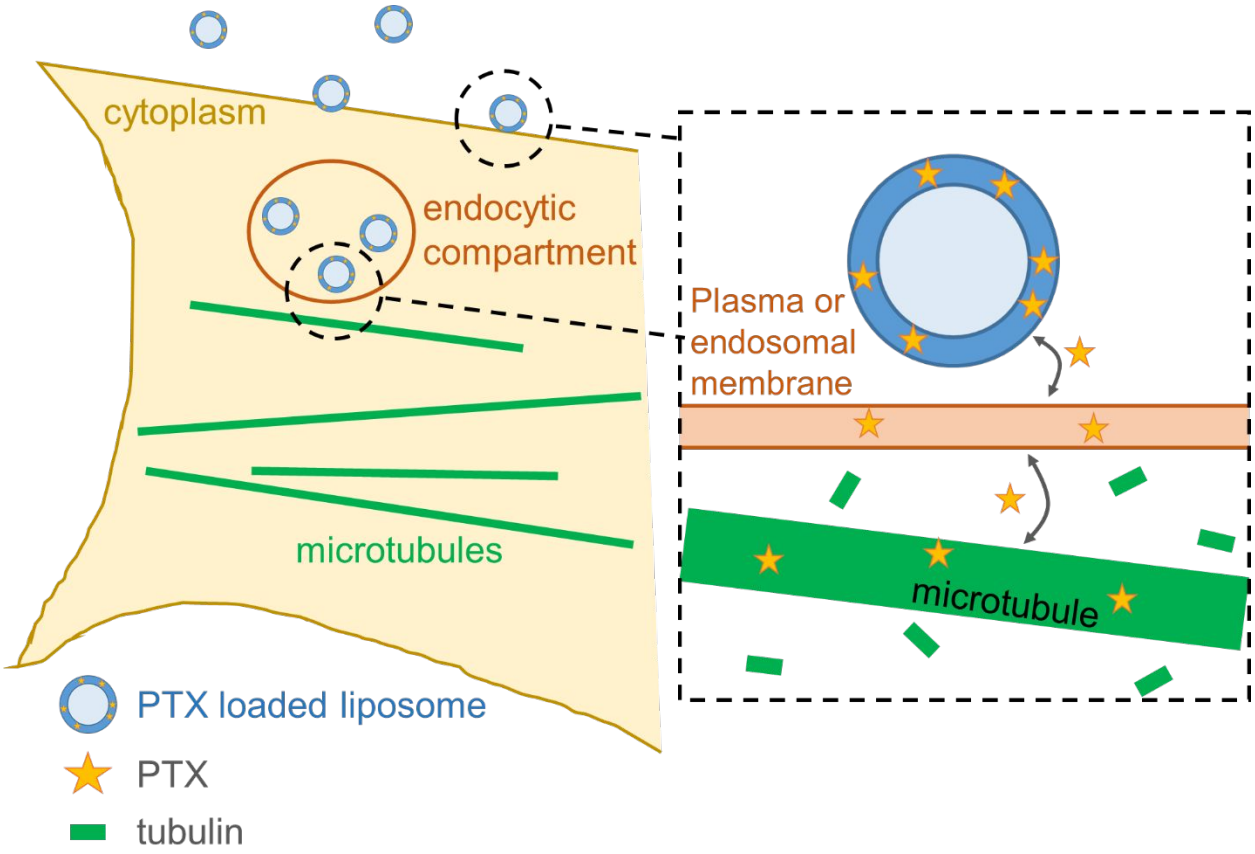

Figure 8. Schematic representation of proposed PTX delivery mechanism from CL_{PTX} NPs. PTX may be able to transfer directly from CL_{PTX} NP to plasma and endosomal membranes without the need for an active release mechanism from the nanoparticle. From there, PTX can interact with tubulin in the cytoplasm.

Interestingly, in 1995 the Torchilin Group first described a generic PEG-lipid micelle system (formulated from a single component PEG-phosphatidylethanolamine) for delivery of hydrophobic drugs[69]. In several subsequent papers they and Krishnadas et al. describe multi-component micelle systems that incorporate egg-phosphatidylcholine and Lipofectin® lipids (cationic) to enhance PTX loading and delivery[70–72]. These results are consistent with our findings that PEG-lipid decreases PTX solubility and further support the advantageous inclusion of cationic lipids in NPs for PTX delivery.

At both the cellular and organismal level, NP size, shape and aspect ratio have been observed to influence cell uptake via endocytosis as well as extravasation from systemic circulation. In *in vivo* intravenous application, non-spherical NPs are advantageous because of margination toward blood vessel walls, which increases the frequency of collisions with blood vessel walls[73]. We did not observe *in vitro* PTX delivery trends that we can directly attribute to shape differences because the bare CL_{PTX} NPs likely aggregated in cell medium and PEG-CL_{PTX} NPs demonstrated similar cell cytotoxicity despite variations in micelle size and shape as a function of charge density. However, CL_{PTX} NP shape may have a greater effect on *in vivo* delivery.

In contrast to a therapeutic agent like nucleic acid (medium to large in size and hydrophilic) the small hydrophobic PTX should be able to diffuse across lipid membranes, and does not appear to need an active release/delivery mechanism into the cell cytoplasm[45]. The two main requirements driving PTX delivery from CLs appear to be adequate solubilization[34] and PTX uptake facilitated by particle stability (maintaining CL_{PTX} NPs at a certain size and shape in complex media). These findings suggest that the reference formulation for these studies, EndoTAG (aka SB05), is not an optimal delivery vehicle for PTX because the drug is loaded at its saturation threshold and, as discussed in this report, because the bare CL_{PTX} NPs are not stabilized. Lessons learned about the importance of drug solubility and particle

stability from this study of PTX may be applicable for development of LNP carriers for other hydrophobic drugs. Further development of PEGylated CL_{PTX} NPs to incorporate targeting ligands could enhance cell-specific uptake and improve this platform as a chemotherapy treatment. Studies in mice (ongoing) will be crucial to determine if the improved *in vitro* PTX uptake from PEG-CL_{PTX} NPs translates to an *in vivo* system.

Supporting Information

Supporting information includes (i) List of cryo-TEM sample compositions and imaging details, (ii) IC-50 fitting parameters, (iii) additional uncropped images of CL NP-treated cells by DIC microscope in fluorescence mode corresponding to Fig. 3 in the main text, (iv) brightfield images used to determine cell boundaries for Fig. 4 in the main text, (v) additional confocal fluorescent images showing horizontal slices at different z heights through cell as well as line scans measuring fluorescence values of PTX_{GF} and $lipid_{RF}$ across cells, (vi) flow cytometry histograms corresponding to data shown in Fig. 5 of the main text, (vii) additional flow cytometry results for CL NPs at different charge densities (30/50/80 mol% DOTAP), (viii) size and charge characteristics of CL NPs measured from cryo-TEM and DLS, (ix) cryo-TEM image showing portion of PTX crystal.

Acknowledgements

This research was supported by the National Institutes of Health under award R01GM130769 (correlating structure to function of drug-carrying nanoparticles). The work was also supported in part by the National Science Foundation under award DMR-1807327 (membrane phase behavior, cryoEM structure studies of lipid nanoparticles). CryoEM experiments were conducted at the Simons Electron Microscopy Center and National Resource for Automated Molecular Microscopy located at the New York Structural Biology Center, supported by grants from the Simons Foundation (SF349247) and the NIH National Institute of

General Medical Sciences (GM103310). The authors acknowledge the use of plate reader and DLS instrument at the Biological Nanostructures Laboratory within the California NanoSystems Institute, supported by the University of California, Santa Barbara and the University of California, Office of the President. We acknowledge the use of the NRI-MCDB Microscopy Facility at the University of California, Santa Barbara for confocal microscopy experiments. VS was supported by the National Science Foundation Graduate Research Fellowship Program under Grant No. DGE 1144085.

References

(1) Wani, M. C.; Taylor, H. L.; Wall, M. E.; Coggon, P.; McPhail, A. T. Plant Antitumor Agents. VI. Isolation and Structure of Taxol, a Novel Antileukemic and Antitumor Agent from Taxus Brevifolia. *J. Am. Chem. Soc.* **1971**, *93*, 2325–2327. https://doi.org/10.1021/ja00738a045.

(2) Jordan, M. A.; Wilson, L. Microtubules as a Target for Anticancer Drugs. *Nat. Rev. Cancer* **2004**, *4*, 253–265. https://doi.org/10.1038/nrc1317.

(3) Weaver, B. A. How Taxol/Paclitaxel Kills Cancer Cells. *Mol. Biol. Cell* **2014**, *25*, 2677–2681. https://doi.org/10.1091/mbc.E14-04-0916.

(4) Wood, A. J. J.; Rowinsky, E. K.; Donehower, R. C. Paclitaxel (Taxol). *N. Engl. J. Med.* **1995**, *332*, 1004–1014. https://doi.org/10.1056/NEJM199504133321507.

(5) Markman, M.; Mekhail, T. M. Paclitaxel in Cancer Therapy. *Expert Opin. Pharmacother.* **2002**, *3*, 755–766. https://doi.org/10.1517/14656566.3.6.755.

(6) Ramalingam, S.; Belani, C. P. Paclitaxel for Non-Small Cell Lung Cancer. *Expert Opin. Pharmacother.* **2004**, *5*, 1771–1780. https://doi.org/10.1517/14656566.5.8.1771.

(7) Hironaka, S.; Zenda, S.; Boku, N.; Fukutomi, A.; Yoshino, T.; Onozawa, Y. Weekly Paclitaxel as Second-Line Chemotherapy for Advanced or Recurrent Gastric Cancer. *Gastric Cancer* **2006**, *9*, 14–18. https://doi.org/10.1007/s10120-005-0351-6.

(8) Sakamoto, J.; Matsui, T.; Kodera, Y. Paclitaxel Chemotherapy for the Treatment of Gastric Cancer. *Gastric Cancer* **2009**, *12*, 69–78. https://doi.org/10.1007/s10120-009-0505-z.

(9) Moxley, K. M.; McMeekin, D. S. Endometrial Carcinoma: A Review of Chemotherapy, Drug Resistance, and the Search for New Agents. *Oncologist* **2010**, *15*, 1026–1033. https://doi.org/10.1634/theoncologist.2010-0087.

(10) World Health Organization. *19th WHO Model List of Essential Medicines*; 2015; Vol. 19.

(11) Yvon, A. M.; Wadsworth, P.; Jordan, M. A. Taxol Suppresses Dynamics of Individual Microtubules in Living Human Tumor Cells. *Mol. Biol. Cell* **1999**, *10*, 947–959.

(12) Dorr, R. T. Pharmacology and Toxicology of Cremophor EL Diluent. *Ann. Pharmacother.* **1994**, *28*, S11–S14.

(13) Gelderblom, H.; Verweij, J.; Nooter, K.; Sparreboom, A. Cremophor EL: The Drawbacks and

Advantages of Vehicle Selection for Drug Formulation. *Eur. J. Cancer* **2001**, *37*, 1590–1598. https://doi.org/10.1016/S0959-8049(01)00171-X.

(14) Bernabeu, E.; Cagel, M.; Lagomarsino, E.; Moretton, M.; Chiappetta, D. A. Paclitaxel: What Has Been Done and the Challenges Remain Ahead. *Int. J. Pharm.* **2017**, *526* (1–2), 474–495. https://doi.org/10.1016/J.IJPHARM.2017.05.016.

(15) Rugo, H. S.; Barry, W. T.; Moreno-Aspitia, A.; Lyss, A. P.; Cirrincione, C.; Leung, E.; Mayer, E. L.; Naughton, M.; Toppmeyer, D.; Carey, L. A.; Perez, E. A.; Hudis, C.; Winer, E. P. Randomized Phase III Trial of Paclitaxel Once Per Week Compared With Nanoparticle Albumin-Bound Nab-Paclitaxel Once Per Week or Ixabepilone With Bevacizumab As First-Line Chemotherapy for Locally Recurrent or Metastatic Breast Cancer: CALGB 40502/NCCTG N0. *J. Clin. Oncol.* **2015**, *33*, 2361–2369. https://doi.org/10.1200/JCO.2014.59.5298.

(16) Gradishar, W. J. Phase III Trial of Nanoparticle Albumin-Bound Paclitaxel Compared With Polyethylated Castor Oil-Based Paclitaxel in Women With Breast Cancer. *J. Clin. Oncol.* **2005**, *23*, 7794–7803. https://doi.org/10.1200/JCO.2005.04.937.

(17) Mahtani, R. L.; Parisi, M.; Glück, S.; Ni, Q.; Park, S.; Pelletier, C.; Faria, C.; Braiteh, F. Comparative Effectiveness of Early-Line Nab-Paclitaxel vs. Paclitaxel in Patients with Metastatic Breast Cancer: A US Community-Based Real-World Analysis. *Cancer Manag. Res.* **2018**, *10*, 249–256. https://doi.org/10.2147/CMAR.S150960.

(18) Wang, F.; Porter, M.; Konstantopoulos, A.; Zhang, P. Preclinical Development of Drug Delivery Systems for Paclitaxel-Based Cancer Chemotherapy. *J. Control. Release* **2017**, *267*, 100–118. https://doi.org/10.1016/J.JCONREL.2017.09.026.

(19) Rosenblum, D.; Joshi, N.; Tao, W.; Karp, J. M.; Peer, D. Progress and Challenges towards Targeted Delivery of Cancer Therapeutics. *Nat. Commun.* **2018**, *9* (1), 1410. https://doi.org/10.1038/s41467-018-03705-y.

(20) Ma, P.; Mumper, R. J. Paclitaxel Nano-Delivery Systems: A Comprehensive Review. *J Nanomed Nanotechnol* **2013**, *4*, 1000164. https://doi.org/10.4172/2157-7439.1000164.

(21) Tibbitt, M. W.; Dahlman, J. E.; Langer, R. Emerging Frontiers in Drug Delivery. *J. Am. Chem. Soc.* **2016**, *138*, 704–717. https://doi.org/10.1021/jacs.5b09974.

(22) Safinya, C. R.; Ewert, K. K. Liposomes Derived from Molecular Vases. *Nature* **2012**, *489* (7416), 372–374. https://doi.org/10.1038/489372b.

(23) Teo, P. Y.; Cheng, W.; Hedrick, J. L.; Yang, Y. Y. Co-Delivery of Drugs and Plasmid DNA for Cancer Therapy. *Adv. Drug Deliv. Rev.* **2016**, *98*, 41–63. https://doi.org/10.1016/J.ADDR.2015.10.014.

(24) Koudelka, Š.; Turánek, J. Liposomal Paclitaxel Formulations. *J. Control. Release* **2012**, *163*, 322–334. https://doi.org/10.1016/j.jconrel.2012.09.006.

(25) Fasol, U.; Frost, A.; Bü Chert, M.; Arends, J.; Fiedler, U.; Scharr, D.; Scheuenpflug, J.; Mross, K. Vascular and Pharmacokinetic Effects of EndoTAG-1 in Patients with Advanced Cancer and Liver Metastasis. *Ann. Oncol.* **2012**, *23*, 1030–1036. https://doi.org/10.1093/annonc/mdr300.

(26) Campbell, R. B.; Ying, B.; Kuesters, G. M.; Hemphill, R. Fighting Cancer: From the Bench to Bedside Using Second Generation Cationic Liposomal Therapeutics. *J. Pharm. Sci.* **2009**, *98* (2), 411–429. https://doi.org/10.1002/JPS.21458.

(27) Strieth, S.; Eichhorn, M. E.; Sauer, B.; Schulze, B.; Teifel, M.; Michaelis, U.; Dellian, M.

Neovascular Targeting Chemotherapy: Encapsulation of Paclitaxel in Cationic Liposomes Impairs Functional Tumor Microvasculature. *Int. J. Cancer* **2004**, *110*, 117–124. https://doi.org/10.1002/ijc.20083.

(28) Strieth, S.; Nussbaum, C. F.; Eichhorn, M. E.; Fuhrmann, M.; Teifel, M.; Michaelis, U.; Berghaus, A.; Dellian, M. Tumor-Selective Vessel Occlusions by Platelets after Vascular Targeting Chemotherapy Using Paclitaxel Encapsulated in Cationic Liposomes. *Int. J. Cancer* **2008**, *122*, 452–460. https://doi.org/10.1002/ijc.23088.

(29) Kunstfeld, R.; Wickenhauser, G.; Michaelis, U.; Teifel, M.; Umek, W.; Naujoks, K.; Wolff, K.; Petzelbauer, P. Paclitaxel Encapsulated in Cationic Liposomes Diminishes Tumor Angiogenesis and Melanoma Growth in a "Humanized" SCID Mouse Model. *J. Invest. Dermatol.* **2003**, *120* (3), 476–482. https://doi.org/10.1046/J.1523-1747.2003.12057.X.

(30) Schmitt-Sody, M.; Strieth, S.; Krasnici, S.; Sauer, B.; Schulze, B.; Teifel, M.; Michaelis, U.; Naujoks, K.; Dellian, M. Neovascular Targeting Therapy: Paclitaxel Encapsulated in Cationic Liposomes Improves Antitumoral Efficacy. *Clin. Cancer Res.* **2003**, *9*, 2335–2341.

(31) Lim, S. B.; Banerjee, A.; Önyüksel, H. Improvement of Drug Safety by the Use of Lipid-Based Nanocarriers. *J. Control. Release* **2012**, *163* (1), 34–45. https://doi.org/10.1016/J.JCONREL.2012.06.002.

(32) Sharma, A.; Mayhew, E.; Bolcsak, L.; Cavanaugh, C.; Harmon, P.; Janoff, A.; Bernacki, R. J. Activity of Paclitaxel Liposome Formulations against Human Ovarian Tumor Xenografts. *Int. J. Cancer* **1997**, *71* (1), 103–107. https://doi.org/10.1002/(SICI)1097-0215(19970328)71:1<103::AID-IJC17>3.0.CO;2-J.

(33) Abraham, S. A.; Waterhouse, D. N.; Mayer, L. D.; Cullis, P. R.; Madden, T. D.; Bally, M. B. The Liposomal Formulation of Doxorubicin. *Methods Enzymol.* **2005**, *391* (SPEC. ISS.), 71–97. https://doi.org/10.1016/S0076-6879(05)91004-5.

(34) Steffes, V. M.; Murali, M. M.; Park, Y.; Fletcher, B. J.; Ewert, K. K.; Safinya, C. R. Distinct Solubility and Cytotoxicity Regimes of Paclitaxel-Loaded Cationic Liposomes at Low and High Drug Content Revealed by Kinetic Phase Behavior and Cancer Cell Viability Studies. *Biomaterials* **2017**, *145*, 242–255. https://doi.org/10.1016/j.biomaterials.2017.08.026.

(35) Campbell, R. B.; Balasubramanian, S. V.; Straubinger, R. M. Influence of Cationic Lipids on the Stability and Membrane Properties of Paclitaxel-containing Liposomes. *J. Pharm. Sci.* **2001**, *90*, 1091–1105. https://doi.org/10.1002/jps.1063.

(36) Bernsdorff, C.; Reszka, R.; Winter, R. Interaction of the Anticancer Agent Taxol (Paclitaxel) with Phospholipid Bilayers. *J. Biomed. Mater. Res.* **1999**, *46*, 141–149. https://doi.org/10.1002/(SICI)1097-4636(199908)46:2<141::AID-JBM2>3.0.CO;2-U.

(37) Sharma, A.; Straubinger, R. M. Novel Taxol Formulations: Preparation and Characterization of Taxol-Containing Liposomes. *Pharm. Res.* **1994**, *11*, 889–896. https://doi.org/10.1023/A:1018994111594.

(38) Castro, J. S.; Tapia, L. V.; Silveyra, R. A.; Martinez, C. A.; Deymier, P. A. Negative Impact of Paclitaxel Crystallization on Hydrogels and Novel Approaches for Anticancer Drug Delivery Systems. In *Current Cancer Treatment - Novel Beyond Conventional Approaches*; Ozdemir, O., Ed.; InTech, 2011; pp 767–782. https://doi.org/10.5772/23372.

(39) Que, C.; Gao, Y.; Raina, S. A.; Zhang, G. G. Z.; Taylor, L. S. Paclitaxel Crystal Seeds with Different Intrinsic Properties and Their Impact on Dissolution of Paclitaxel-HPMCAS Amorphous

Solid Dispersions. *Cryst. Growth Des.* **2018**, *18* (3), 1548–1559. https://doi.org/10.1021/acs.cgd.7b01521.

(40) Campbell, R. B.; Fukumura, D.; Brown, E. B.; Mazzola, L. M.; Izumi, Y.; Jain, R. K.; Torchilin, V. P.; Munn, L. L. Cationic Charge Determines the Distribution of Liposomes between the Vascular and Extravascular Compartments of Tumors. *Cancer Res.* **2002**, *62*, 6831–6836.

(41) Eichhorn, M. E.; Ischenko, I.; Luedemann, S.; Strieth, S.; Papyan, A.; Werner, A.; Bohnenkamp, H.; Guenzi, E.; Preissler, G.; Michaelis, U.; Jauch, K.; Bruns, C. J.; Dellian, M. Vascular Targeting by EndoTAG™-1 Enhances Therapeutic Efficacy of Conventional Chemotherapy in Lung and Pancreatic Cancer. *Int. J. Cancer* **2010**, *126*, 1235–1245. https://doi.org/10.1002/ijc.24846.

(42) Thurston, G.; Mclean, J. W.; Rizen, M.; Baluk, P.; Haskell, A.; Murphy, T. J.; Hanahan, D.; Mcdonald, D. M. Cationic Liposomes Target Angiogenic Endothelial Cells in Tumors and Chronic Inflammation in Mice. *J. Clin. Invest* **1998**, *101*, 1401–1413.

(43) Bode, C.; Trojan, L.; Weiss, C.; Kraenzlin, B.; Michaelis, U.; Teifel, M.; Alken, P.; Michel, M. S. Paclitaxel Encapsulated in Cationic Liposomes: A New Option for Neovascular Targeting for the Treatment of Prostate Cancer. *Oncol. Rep.* **2009**, *22*, 321–326.

(44) Ho, E. A.; Ramsay, E.; Ginj, M.; Anantha, M.; Bregman, I.; Sy, J.; Woo, J.; Osooly-Talesh, M.; Yapp, D. T.; Bally, M. B. Characterization of Cationic Liposome Formulations Designed to Exhibit Extended Plasma Residence Times and Tumor Vasculature Targeting Properties. *J Pharm Sci* **2010**, *99*, 2839–2853. https://doi.org/10.1002/jps.22043.

(45) Allen, T. M.; Cullis, P. R. Liposomal Drug Delivery Systems: From Concept to Clinical Applications. *Adv. Drug Deliv. Rev.* **2013**, *65*, 36–48. https://doi.org/10.1016/j.addr.2012.09.037.

(46) Allen, T. M.; Hansen, C. B.; de Menezes, D. E. L. Pharmacokinetics of Long-Circulating Liposomes. *Adv. Drug Deliv. Rev.* **1995**, *16* (2–3), 267–284. https://doi.org/10.1016/0169-409X(95)00029-7.

(47) Kenworthy, A. K.; Hristova, K.; Needham, D.; McIntosh, T. J. Range and Magnitude of the Steric Pressure between Bilayers Containing Phospholipids with Covalently Attached Poly(Ethylene Glycol). *Biophys. J.* **1995**, *68* (5), 1921–1936. https://doi.org/10.1016/S0006-3495(95)80369-3.

(48) Marsh, D.; Bartucci, R.; Sportelli, L. Lipid Membranes with Grafted Polymers: Physicochemical Aspects. *Biochim. Biophys. Acta - Biomembr.* **2003**, *1615* (1–2), 33–59. https://doi.org/10.1016/S0005-2736(03)00197-4.

(49) Majzoub, R. N.; Chan, C.-L.; Ewert, K. K.; Silva, B. F. B.; Liang, K. S.; Jacovetty, E. L.; Carragher, B.; Potter, C. S.; Safinya, C. R. Uptake and Transfection Efficiency of PEGylated Cationic Liposome–DNA Complexes with and without RGD-Tagging. *Biomaterials* **2014**, *35*, 4996–5005. https://doi.org/10.1016/j.biomaterials.2014.03.007.

(50) Cullis, P. R.; Hope, M. J. Lipid Nanoparticle Systems for Enabling Gene Therapies. *Mol. Ther.* **2017**, *25* (7), 1467–1475. https://doi.org/10.1016/J.YMTHE.2017.03.013.

(51) Hatakeyama, H.; Akita, H.; Harashima, H. A Multifunctional Envelope Type Nano Device (MEND) for Gene Delivery to Tumours Based on the EPR Effect: A Strategy for Overcoming the PEG Dilemma. *Adv. Drug Deliv. Rev.* **2011**, *63* (3), 152–160. https://doi.org/10.1016/J.ADDR.2010.09.001.

(52) Pollard, T. D.; Earnshaw, W. C.; Lippincott-Schwartz, J.; Johnson, G. T. *Cell Biology*, 3rd ed.; Elsevier: Philadelphia, 2017.

(53) Matsumura, Y.; Maeda, H. A New Concept for Macromolecular Therapeutics in Cancer Chemotherapy: Mechanism of Tumoritropic Accumulation of Proteins and the Antitumor Agent Smancs. *Cancer Res.* **1986**, *46*, 6387–6392.

(54) Wonder, E.; Simón-Gracia, L.; Scodeller, P.; Majzoub, R. N.; Kotamraju, V. R.; Ewert, K. K.; Teesalu, T.; Safinya, C. R. Competition of Charge-Mediated and Specific Binding by Peptide-Tagged Cationic Liposome–DNA Nanoparticles in Vitro and in Vivo. *Biomaterials* **2018**, *166*, 52–63. https://doi.org/10.1016/j.biomaterials.2018.02.052.

(55) Ewert, K. K.; Kotamraju, V. R.; Majzoub, R. N.; Steffes, V. M.; Wonder, E. A.; Teesalu, T.; Ruoslahti, E.; Safinya, C. R. Synthesis of Linear and Cyclic Peptide–PEG–Lipids for Stabilization and Targeting of Cationic Liposome–DNA Complexes. *Bioorg. Med. Chem. Lett.* **2016**, *26* (6), 1618–1623. https://doi.org/10.1016/J.BMCL.2016.01.079.

(56) Biswas, S.; Dodwadkar, N. S.; Deshpande, P. P.; Torchilin, V. P. Liposomes Loaded with Paclitaxel and Modified with Novel Triphenylphosphonium-PEG-PE Conjugate Possess Low Toxicity, Target Mitochondria and Demonstrate Enhanced Antitumor Effects in Vitro and in Vivo. *J. Control. Release* **2012**, *159* (3), 393–402. https://doi.org/10.1016/J.JCONREL.2012.01.009.

(57) MacEwan, S. R.; Chilkoti, A. Harnessing the Power of Cell-Penetrating Peptides: Activatable Carriers for Targeting Systemic Delivery of Cancer Therapeutics and Imaging Agents. *Wiley Interdiscip. Rev. Nanomed. Nanobiotechnol.* **2013**, *5* (1), 31–48. https://doi.org/10.1002/wnan.1197.

(58) Schulze, U.; Schmidt, H.-W.; Safinya, C. R. Synthesis of Novel Cationic Poly(Ethylene Glycol) Containing Lipids. *Bioconjug. Chem.* **1999**, *10* (3), 548–552. https://doi.org/10.1021/BC9801068.

(59) Sofias, A. M.; Dunne, M.; Storm, G.; Allen, C. The Battle of "Nano" Paclitaxel. *Adv. Drug Deliv. Rev.* **2017**, *122*, 20–30. https://doi.org/10.1016/j.addr.2017.02.003.

(60) Zidovska, A.; Ewert, K. K.; Quispe, J.; Carragher, B.; Potter, C. S.; Safinya, C. R. Block Liposome and Nanotube Formation Is a General Phenomenon of Two-Component Membranes Containing Multivalent Lipids. *Soft Matter* **2011**, *7* (18), 8363–8369. https://doi.org/10.1039/C1SM05481C.

(61) Zidovska, A.; Ewert, K. K.; Quispe, J.; Carragher, B.; Potter, C. S.; Safinya, C. R. The Effect of Salt and PH on Block Liposomes Studied by Cryogenic Transmission Electron Microscopy. *Biochim. Biophys. Acta - Biomembr.* **2009**, *1788* (9), 1869–1876. https://doi.org/10.1016/J.BBAMEM.2009.06.013.

(62) Zidovska, A.; Ewert, K. K.; Quispe, J.; Carragher, B.; Potter, C. S.; Safinya, C. R. Block Liposomes from Curvature-Stabilizing Lipids: Connected Nanotubes, -Rods, or -Spheres. *Langmuir* **2009**, *25* (5), 2979–2985. https://doi.org/10.1021/la8022375.

(63) Crosasso, P.; Ceruti, M.; Brusa, P.; Arpicco, S.; Dosio, F.; Cattel, L. Preparation, Characterization and Properties of Sterically Stabilized Paclitaxel-Containing Liposomes. *J. Control. Release* **2000**, *63*, 19–30. https://doi.org/10.1016/S0168-3659(99)00166-2.

(64) Israelachvili, J. N. *Intermolecular and Surface Forces*; Academic Press, 2011.

(65) Bergström, L. M. Bending Energetics of Tablet-Shaped Micelles: A Novel Approach to Rationalize Micellar Systems. *ChemPhysChem* **2007**, *8* (3), 462–472. https://doi.org/10.1002/cphc.200600692.

(66) Helfrich, W. Elastic Properties of Lipid Bilayers: Theory and Possible Experiments. *Z. Naturforsch. C.* **1973**, *28* (11), 693–703.

(67) Lipowsky, R.; Sackmann, E. *Structure and Dynamics of Membranes*; Elsevier: Amsterdam, 1995.

(68) Safran, S. A. *Statistical Thermodynamics of Surfaces, Interfaces, and Membranes*; Addison-Wesley Pub, 1994.

(69) Trubetskoy, V. S.; Torchilin, V. P. Use of Polyoxyethylene-Lipid Conjugates as Long-Circulating Carriers for Delivery of Therapeutic and Diagnostic Agents. *Adv. Drug Deliv. Rev.* **1995**, *16* (2–3), 311–320. https://doi.org/10.1016/0169-409X(95)00032-3.

(70) Krishnadas, A.; Rubinstein, I.; Önyüksel, H. Sterically Stabilized Phospholipid Mixed Micelles: In Vitro Evaluation as a Novel Carrier for Water-Insoluble Drugs. *Pharm. Res.* **2003**, *20* (2), 297–302.

(71) Gao, Z.; Lukyanov, A. N.; Singhal, A.; Torchilin, V. P. Diacyllipid-Polymer Micelles as Nanocarriers for Poorly Soluble Anticancer Drugs. *Nano Lett.* **2002**, *2* (9), 979–982. https://doi.org/10.1021/NL025604A.

(72) Wang, J.; Mongayt, D.; Torchilin, V. P. Polymeric Micelles for Delivery of Poorly Soluble Drugs: Preparation and Anticancer Activity *in Vitro* of Paclitaxel Incorporated into Mixed Micelles Based on Poly(Ethylene Glycol)-Lipid Conjugate and Positively Charged Lipids. *J. Drug Target.* **2005**, *13* (1), 73–80. https://doi.org/10.1080/10611860400011935.

(73) Kinnear, C.; Moore, T. L.; Rodriguez-Lorenzo, L.; Rothen-Rutishauser, B.; Petri-Fink, A. Form Follows Function: Nanoparticle Shape and Its Implications for Nanomedicine. *Chem. Rev.* **2017**, *117* (17), 11476–11521. https://doi.org/10.1021/acs.chemrev.7b00194.

For Table of Contents Only